ingegneria sismica
International Journal of Earthquake Engineering
Anno XLIII - Num. 2 - 2026

# Study on the Nanostructure Control and Acid Corrosion Resistance Mechanism of Fluorosilicon-Modified Epoxy Resin Coatings

*Fei Liu*[1] *and Xin Wang*[2,*]

[1] Leadship, Shandong Nuclear Power Company, 265116, Yantai, China
[2] Technical Support Department, Shandong Nuclear Power Company, 265116, Yantai, China

**SUMMARY:** *For solving the problems of liquid absorbing and plasticization, interface layering, and corrosion below film which epoxy resin coatings often meet in acidic working environments, this research has prepared a reactive fluorosilicon low polymer that can co-solidify with epoxy systems, and systematically studied its adjustment functions on the nano-structure and acid corrosion resistance of the coatings. Through the control of fluorosilicon content, the surface enrichment, size of nano-phase domains, surface energy, crosslinking density, acid absorption, electrochemical response, and failure morphology after immersion have been compared for coatings that have different formulations. Furthermore, quantitative interrelations among structure parameters and long-term impedance holding were established through the utilization of AFM, XPS, DMA, and EIS. The outcomes show that fluorosilicon compositions can form a surface layer with much fluorine and silicon in the curing process, and enhance the diffusion curvature inside the membrane, therefore the 6 wt% formula displays the best comprehensive performance: the water contact angle increased to 112.8°, the surface free energy decreased to 19.6 $mN{\cdot}m^{-1}$, acid absorption rate after 30* d *decreased to 2.87%, and the apparent diffusion coefficient decreased to $7.6\times10^{-10} cm^{2}{\cdot}s^{-1}$; in 0.1 $mol{\cdot}L^{-1} H_2SO_4$, its $|Z|_{0.01Hz}$ remained at $7.90\times10^{6}\ \Omega{\cdot}cm^{2}$ after 30* d*, the corrosion current density was only $3.92\times10^{-8} A{\cdot}cm^{-2}$, and the adhesion retention rate reached 86.5%, demonstrating the best overall acid resistance.Mechanism analysis indicates that the enhanced acid resistance stems from the synergistic effects of a stable low-energy surface layer, an appropriate distribution of nanostructures, and a continuous cross-linked network, whereas an excess of fluorosilicon weakens the long-term barrier effect due to coarsening of the phase regions. This study provides a basis and reference for the formulation design and mechanism analysis of epoxy protective coatings in acidic media, which can be directly applied to engineering screening, failure diagnosis, and formulation scaling.*

***KEYWORDS:*** *fluorosilicon modification; epoxy coating; nanostructure; acid corrosion resistance; electrochemical impedance spectroscopy*

## 1 Introduction

Heavy-load protection situations inside acid environments are subjected to strict engineering restriction conditions. Acid washing production lines, hydrometallurgy reaction troughs, flue gas desulfurization (FGD) circulating devices, chemical acid holding tanks, and acid mist conveying pipe systems are endured by the combined influences of low pH, uninterrupted wetting, ion movement, and temperature changes over long time periods. For steel substrates,

*wangxin07@spic.com.cn
https://doi.org/10.65102/is20261016
Published: 30 April, 2026

once the coating loses its barrier function, interfacial reactions rapidly amplify in defect zones, subsequently leading to blistering, delamination, and under-film corrosion. Maintenance costs are significantly higher than those for general protective applications in neutral environments. Due to their high adhesion, mature compatibility systems, and wide application window, epoxy resin coatings remain one of the most commonly used organic protective systems for such equipment [1, 2]. However, the hydroxyl groups, ether bonds, and amine-cured structures within the epoxy network possess strong polarity. Additionally, the cured film inevitably contains free volume and locally non-uniform regions. Upon prolonged contact with acidic media, acids readily adsorb at these polar sites, diffuse through the network voids, and induce plasticization, chemical bond breakage, and the cumulative coupling of interfacial electrochemical reactions. Therefore, the design focus of acid-resistant epoxy systems should not be limited to improving initial hardness or film thickness; more crucially, it should aim to reduce surface wetting during the early service life, delay migration within the film during the middle stage, and suppress the expansion of interfacial reactions in the later stage.

When we make a comparison with marine salt spray or traditional atmospheric corrosion, hence the time scale of failure in acidic medium is shorter, and the condition of interface is more sensitive. Coating layers can have quality alterations, a drop in modulus values, and adhesion capability deterioration inside a short time frame; Traditional screening methods which depend on long-period salt spray tests have difficulty in quickly finding structure problems in preparation formulas. Hence, the research that aims at acidic environments must with equal importance analyze "early wetting behavior" and "mid-to-late-stage interfacial reactions", therefore keeping the quantitative evaluation of the structural integrity of films.

To achieve this goal, fluorinated and organosilicon structures are currently the two most representative types of modifying units. Fluorinated segments possess low polarizability and high bond energy, which can reduce the surface free energy of the coating, weaken the adsorption tendency of acidic solutions and polar media on the surface, and to some extent enhance the material’s chemical stability;Silicone segments, on the other hand, possess low surface tension, high flexibility, and a relatively stable Si-O-Si backbone, which can improve interfacial wetting conditions, mitigate local stress concentration, and enhance the film’s weather resistance and barrier properties through an inorganic skeleton [3, 4]. In reactive designs, these two types of structures also have the potential to simultaneously participate in the construction of the curing network, thereby unifying surface energy reduction and bulk structural stability within a single formulation.

Acidic environments impose stricter mechanistic requirements on such designs. Existing research indicates that amine-cured epoxies undergo a complex process in acids involving simultaneous adsorption, diffusion, plasticization, and chemical degradation; the degradation of coating performance is not merely a simple “liquid absorption and weight gain,” but is accompanied by the gradual accumulation of network relaxation, changes in dielectric response, and interfacial reactions [5]. At the same time, the stability of fluorinated surface layers in acidic, alkaline, and saline environments is not entirely consistent; if the reduction in surface energy is not matched by the structure of the continuous film layer, the advantages during long-term service will rapidly diminish [6]. This implies that acid-resistant epoxy systems cannot be evaluated solely based on static contact angles or short-term immersion phenomena, but must also consider surface retention, in-film transport, and interfacial evolution.

The direction of related research has thus also had a change in recent years. Quite a number of researches have made attempts to further decrease liquid attachment and interface staying time through using superhydrophobic micro-structures and nano-structures, therefore other researches have chosen reactive fluorine-containing or silicon-containing monomers to decrease the movement and losing of low-surface-energy constituents in long-time use [7-11].

This indicates that the field has gradually shifted from the approach of “achieving short-term effects through externally added hydrophobic components” to the approach of “obtaining stable interfaces through chemical bonding and network design.” This shift is particularly significant in acidic environments. The destruction of covering layers by acid liquids frequently starts with continuous soaking and partial ion gathering inside an extremely thin interface layer. If the low-surface-energy layer is not able to keep stability, therefore, the original good points will rapidly be covered by diffusion and interface reactions; when the network has no enough continuous property, quick channels can still be formed inside the thin film even though the surface contact angle is at a relatively high level. Just to say this, systems which do not get corroded by acid need both “surface stability” and “volume stability” to get reached at the same time.

However, the currently existing studies about fluorosilicon-modified epoxy under acidic environments still have a number of key gaps. First, most studies focus performance evaluations on salt spray, neutral NaCl, or room-temperature static immersion systems; data directly addressing long-term immersion in acidic media, charge transfer, and the evolution of under-film corrosion remain insufficient.Second, regarding the synergistic effects of fluorine and silicon, many reports remain at the formulation level, with discussions primarily focused on contact angles, surface roughness, or impedance values at a specific point in time. There is a lack of systematic analysis of the coupling relationship between the scale of the nano-phase regions in the cured film, the degree of surface migration, and network continuity.If the migration of fluorosilicon segments is insufficient, it is difficult to establish a low-energy surface layer; if migration is too strong or compatibility is insufficient, coarse phase regions and localized flexible enrichment zones may form, which conversely provide preferential penetration pathways for acidic media. Third, mechanistic explanations often conclude with improved hydrophobicity, lacking continuous evidence spanning from nanostructure, diffusion coefficients, and electrochemical fitting parameters to failure morphology. Consequently, it is difficult to accurately define the optimal window for fluorosilicon addition, and it is also difficult to explain why some high-contact-angle formulations still experience rapid degradation after long-term immersion.

For formulation design targeting acidic operating conditions, the aforementioned gaps ultimately boil down to two more specific questions. First, what kind of surface-enriched layer and bulk nanostructure are actually formed during the curing process after reactive fluorosilicon oligomers are introduced into the epoxy system;Second, through which pathways does this structure influence the wetting, absorption, diffusion, and interfacial reactions of the acidic medium? If surface energy reduction and bulk densification can be established simultaneously, the coating is expected to reduce acid spreading during the initial contact stage, increase migration curvature during the diffusion stage, and delay the formation of corrosion cells during the interfacial stage; if the two processes are out of sync, improvements in surface properties may be offset by bulk defects.Based on this logic, it is necessary to examine surface element distribution, phase domain size, thermomechanical parameters, acid absorption behavior, electrochemical response, and post-corrosion morphology within a unified framework to provide a compelling explanation for the acid resistance mechanism of fluorosilicon-modified epoxy.

Based on this, this study uses bisphenol A-type epoxy resin as the matrix to formulate a reactive fluorosilicon oligomer capable of co-curing with it, and prepares a series of coating samples with varying loading levels. The research first characterizes the regulation mechanisms of the fluorosilicon component on surface enrichment, nano-phase domains, surface energy, and cross-linking networks using FTIR, XPS, AFM, contact angle, and DMA. After that, acid absorption experiments, 5 weight percent $H_2SO_4$ dipping, electrochemistry impedance spectrum analysis, dynamic voltage current polarization measurement, adhesive retention ratio, and after-

corrosion shape observation are used to assess their blocking capability and invalidation mechanisms inside acid environments. The core focus of this study is not merely to compare which formulation is “more hydrophobic,” but to establish a correlation between fluorosilicon content, nanostructure, and acid corrosion resistance, and thereby explain the formation of the optimal acid resistance window.The main contributions of this paper are threefold: first, it provides structural evidence for the formation of a surface layer enriched in fluorine and silicon and a continuous bulk network within the epoxy-cured film by reactive fluorosilicon oligomers; second, it quantitatively reveals the effects of varying fluorosilicon content on acid absorption, diffusion coefficients, impedance retention, and corrosion current density;third, it proposes a framework for failure pathways and suppression mechanisms in acidic media, providing a basis for engineering decisions in the formulation optimization of fluorosilicon-modified epoxy coatings.

# 2 Methods

## 2.1 Preparation of Fluorosilicone-Modified Epoxy Coating System

Bisphenol A-type epoxy resin E-51 was selected as the matrix resin, with an epoxy value of 0.51-0.54 eq/100 g; polyetheramine D230 was chosen as the curing agent to balance workability during the room-temperature pre-curing stage with network densification capability during the medium-temperature post-curing stage.To introduce low-surface-energy silyl structures capable of co-curing into the epoxy matrix, this study employed 3-glycidylpropyltrimethoxysilane (GPTMS), methyltrimethoxysilane (MTMS), and 3,3,3-trifluoropropyltrimethoxysilane (TFPTMS) to prepare reactive fluorosilicone oligomers(FSO). Among these, GPTMS provides reactive end groups capable of integrating into the epoxy/amine crosslinking system, serving to enhance the chemical anchoring between the fluorosilicon component and the host resin; MTMS is primarily used to improve the continuity of the siloxane backbone and the stability of the condensation reaction; TFPTMS provides trifluoropropyl segments to induce the directional enrichment of low-energy surface groups during curing.All reagents were of analytical grade and were stored in a sealed container in a dry environment prior to use. Q235 steel plates (100 mm × 50 mm × 2 mm) were used for electrochemical testing and acid immersion experiments, while glass plates and polytetrafluoroethylene (PTFE) molds were used to prepare flat-surface coatings and free-standing film specimens, respectively.

The FSO oligomer has been obtained through one controlled sol-gel method path. Firstly, GPTMS, MTMS and TFPTMS were mixed together with a mole proportion of 2:4:4, and anhydrous ethyl alcohol was then added. This mixture was stirred by machine for 20 minutes under 45 °C in order to guarantee that the precursors get the sufficient homogeneous mixing. After that, a mixture made from deionized water, ethanol, and glacial acetic acid got prepared, with the molar ratio of water to all alkoxy groups in this system being controlled at 1.2:1 to reduce fast gelation that is brought by overmuch condensation. This mixed liquid was slowly added one drop by one drop into the silane reaction system, keeping a pH value of 4.0 ± 0.2, and the reaction was continuously carried out for 3 hours to let the system preferentially finish the hydrolysis of Si-$OCH_3$ hydrolysis and the production of a preliminary Si-O-Si condensation structure. When the reaction was finished, components with low boiling point were gotten rid of by decompression at 60 °C and -0.08 MPa, therefore a pale yellow, see-through FSO oligomer was obtained. In order to reduce to the greatest extent the composition changes which are brought by secondary condensation in the storage period, the obtained FSO must be placed

still at room temperature through 24 hours, before it is used for the follow-up preparation of preparations.

In terms of formulation design, the proportion of FSO relative to the total resin mass was set at 0, 2, 4, 6, and 8 wt%; the corresponding samples were designated as EP-0, FS-2, FS-4, FS-6, and FS-8.To prepare the coatings, E-51 and a measured amount of FSO were first stirred at 60 °C for 30 min to promote the uniform dispersion of the fluorosilicon oligomer in the epoxy resin; this was followed by 15 min of vacuum degassing to reduce microbubbles introduced by the pre-polymerized siloxane structures.D230 was then added based on an equivalent ratio of epoxy groups to active hydrogen of 1.00:0.95, and stirring was continued at low speed for 10 min.This study employs a slightly stoichiometrically deficient amine dosage, primarily for two reasons: first, to reduce the polar contribution of residual free amine in acidic media; second, to help suppress the adhesion decay caused by localized hydration enhancement following interfacial water absorption [12-16].

To facilitate comparison of the effects of different FSO loading levels on film-forming behavior, interfacial state, and acid resistance, the base formulations and application parameters for each sample group are uniformly listed in Table 1. Table 1 presents the settings for the main resin, FSO, curing agent, and solvent in the five sample groups (EP-0 to FS-8), as well as the uniformly controlled dry film thickness range.Subsequent comparisons of differences in structural characterization, electrochemical impedance, polarization response, acid absorption, and adhesion retention rate are all based on the formulations listed in this table.

*Table 1: Making scheme of fluorosilicone-modified epoxy paint layers*

| Sample | E-51 / wt% | FSO / wt% | D230 / phr | Solvent / wt% | Dry film thickness / μm |
|---|---|---|---|---|---|
| EP-0 | 100 | 0 | 32 | 8 | 80±5 |
| FS-2 | 98 | 2 | 32 | 8 | 80±5 |
| FS-4 | 96 | 4 | 32 | 8 | 80±5 |
| FS-6 | 94 | 6 | 32 | 8 | 80±5 |
| FS-8 | 92 | 8 | 32 | 8 | 80±5 |

In Table 1, each formulation features a gradient adjustment of the FSO content only, with the amount of E-51 decreasing proportionally, while the amount of D230, the total solvent mass fraction, and the dry film thickness remain constant. This approach serves two purposes. First, it focuses the variables on the amount of fluorosilicon component introduced, thereby avoiding interference in the interpretation of results caused by fluctuations in curing agents, differences in solvents, and variations in film thickness.Second, controlling the dry film thickness at 80 ± 5 μm helps minimize the impact of variations in diffusion path length on acid transport behavior, thereby ensuring that subsequent changes in acid resistance more accurately correspond to alterations in network structure, surface enrichment, and microphase morphology.It should be noted that the 0-8 wt% formulation window was not simply set at equal intervals but was determined based on preliminary experimental observations: when FSO was below 2 wt%, the contact angle increase was weak, and the F signal in the XPS surface analysis was not significant; when the content exceeded 8 wt%, the application viscosity increased significantly, and localized pinholes and microscale shrinkage patterns were more likely to appear during the leveling stage.Therefore, this study employs a 2 wt% increment to establish a series of samples, aiming to identify the complete range of changes in acid resistance from insufficient introduction, through gradual optimization, to excessive incorporation.

The covering was spread on the sandblasted plane of Q235 steel sheets by means of a squeegee way. The sand-blasting rank was controlled as Sa 2.5, and the surface coarse degree Ra was kept at 25-35 μm. Before the coating work was carried out, the steel plates were in order

degreased by acetone, cleaned by anhydrous ethanol, and dried by hot air. The coating work was finished within two hours after sandblasting, in order to reduce the influence that moisture and the second-time adsorption of impurities from the air have on the interface state. The thickness of the wet film was controlled to be 120 ± 10 μm. After being placed to level at room temperature for 20 minutes, the coating was carried out pre-curing at 25 °C for 24 hours, and was followed by post-curing at 80 °C for 2 hours, which therefore gives a final dry film thickness of 80 ± 5 μm. For enabling the minimization of the influence that differences in solvent evaporation speed bring to surface movement, the total mass percentage of solvent content in all preparation schemes was uniformly controlled at 8 wt%. The application environment's temperature we kept at 23-25 °C, and the relative humidity is held below 50%. All samples were placed at room temperature through 7 d before the final testing to guarantee that post-polymerization and post-curing were basically finished, therefore reducing extra variables which are brought by differences in curing degree.

The surface condition of the substrate directly affects interfacial bond strength and subsequent acid immersion results; therefore, a standardized screening and documentation process was implemented for the steel plates in this study. Surface roughness and initial mass were recorded for each steel plate, and samples with mechanical damage at the edges were excluded.After complete curing, the free-film specimens were slowly peeled along the edges, then cut into 20 mm × 20 mm test pieces, and vacuum-dried at 50 °C until constant weight prior to testing. To ensure cross-correlation between different test results, both the coated plates and free-film specimens under the same formulation were prepared from the same batch of samples, thereby minimizing the interference of batch-to-batch variations on the correlation between structural parameters, electrochemical parameters, and immersion parameters.

To ensure consistency in subsequent charts and result analysis, this study uniformly designated sample numbers, formulations, and test subjects during the experimental phase. The thickness of the free-standing film was measured at 10 locations using a micrometer, and the average value was calculated;electrochemical specimens were encapsulated in epoxy insulation, leaving only a 1.0 $cm^2$ exposed area; for AFM, contact angle, and XPS characterization, samples free of pinholes and sagging that had stabilized after 7 d of curing were prioritized. The formation pathway of the fluorosilicone oligomer, its co-curing incorporation mechanism, and its barrier function in an acidic medium are shown in Figure 1.

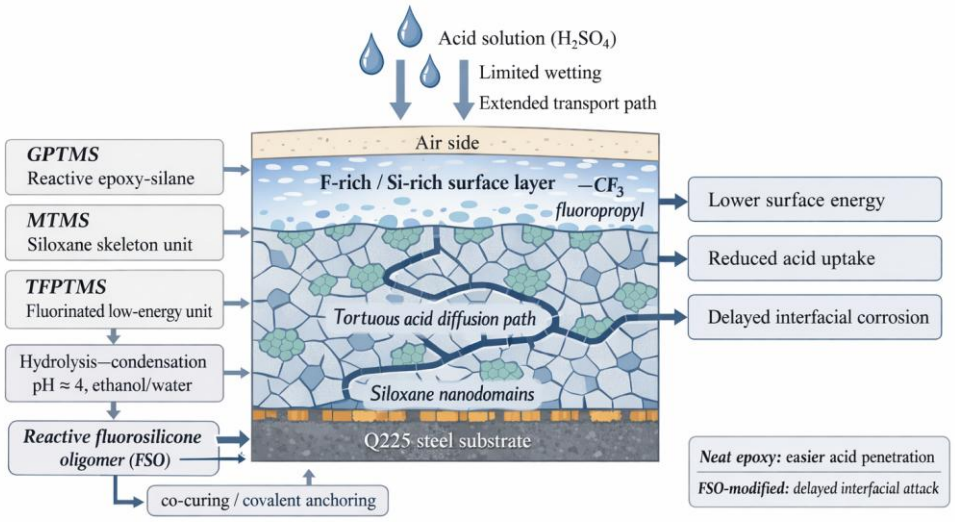


*Figure 1: Formation and acid-barrier mechanism of fluorosilicone-modified epoxy coating.*

Figure 1 illustrates, on the one hand, the relationship between the hydrolytic condensation of FSO and the co-curing of the epoxy network; on the other hand, it demonstrates the corresponding mechanisms between the surface fluorine- and silicon-rich layer, the bulk cross-linked structure, and the acid diffusion pathway, providing a methodological foundation for subsequent analyses of surface energy, electrochemical impedance, and acid-induced failure behavior.

## 2.2 Curing, joint preparation, and acid-thermal aging protocol

To identify the distribution of fluorine and silicon components in the cured film, this study employs an integrated characterization approach linking "chemical structure-surface composition-nanophase regions-thermomechanical response." FTIR was used to confirm the successful introduction of the siloxane backbone and fluorinated segments, with a testing range of 4000-500 $cm^{-1}$, a resolution of 4 $cm^{-1}$, and a total of 32 scans.XPS was used to characterize the elemental composition and chemical state of the surface layer within the 5-10 nm region, with a focus on the C 1s, O 1s, Si 2p, and F 1s peaks; the degree of fluorine and silicon enrichment was quantified using surface atomic fractions.AFM was performed in phase mode with a fixed scan area of 5 μm × 5 μm; surface phase region size, area fraction, and root-mean-square roughness Ra were statistically analyzed via image threshold segmentation. SEM was used to observe surface defects and cross-sectional delamination before and after corrosion, with cross-sectional samples gold-sputtered after brittle fracture in liquid nitrogen.Contact angle measurements were performed using deionized water and ethylene glycol as probe liquids. Five different locations were selected on each sample, and the average was calculated after three single-point measurements at each location.DMA was conducted in tensile mode at a heating rate of 3 °C·$min^{-1}$and a frequency of 1 Hz to determine the storage modulus, loss peak position, and glass transition temperature. Surface free energy was calculated using the Owens-Wendt two-liquid method for each probe liquid, as shown in Equation (1).

$$\gamma_l(1+\cos\theta)=2\left(\sqrt{\gamma_s^d\gamma_l^d}+\sqrt{\gamma_s^p\gamma_l^p}\right) \tag{1}$$

where $\gamma_l$ is the surface tension of the probe solution, $\gamma_l^d$ and $\gamma_l^p$ are its dispersive and polar components, respectively; $\gamma_s$ is the surface free energy of the solid, $\gamma_s^d$ and $\gamma_s^p$ are the dispersive and polar components of the solid surface, respectively; and $\theta$ is the equilibrium contact angle. This parameter is used to assess changes in surface polarity and wetting characteristics following the introduction of fluorosilicon, and corresponds to subsequent behavior upon contact with acidic solutions.

Crosslinking density is no longer calculated separately but is estimated from the storage modulus in the rubber plateau region above the glass transition temperature in the DMA curve to minimize the interference of fluctuations in the glass transition region on the results [17-20]. The acid absorption rate is determined using the free-film weight gain method, expressed as the percentage of the difference between the pre-immersion mass and the mass at each time point relative to the initial mass; the surface element retention rate is expressed as the ratio of the post-immersion surface F or Si atomic fraction relative to the initial value, and is used to evaluate the stability of the fluorine- and silicon-rich layer in acidic media. All of the above parameters are statistically analyzed using three or more parallel samples, and the results are expressed as the mean ± standard deviation.

The apparent diffusion capacity of the acid medium within the membrane was determined by fitting the Fick approximation during the initial absorption phase. For the stage where $\frac{Q_t}{Q_\infty} < 0.6$, as shown in Equation (2).

$$\frac{Q_t}{Q_\infty} = 4\left(\frac{Dt}{\pi L^2}\right)^{1/2} \tag{2}$$

where $Q_t$ is the acid absorption rate at immersion time $t$, $Q_\infty$ is the equilibrium absorption rate, $D$ is the apparent diffusion coefficient, and $L$ is the free membrane thickness.In this study, a least-squares fit was performed using data segments from the first 72 h that satisfied a linear relationship, to mitigate the influence of later-stage film plasticization and interfacial reactions on diffusion estimates. Considering that the acid solution may cause local irreversible chemical changes, the $D$ provided in this paper is used solely as an apparent transport parameter and is not equated with the intrinsic diffusion coefficient in an ideal homogeneous film.

In addition to individual parameters, this study focuses on the correlations among structural parameters. AFM phase-region sizes were statistically derived from at least 50 independent regions and expressed as equivalent circular diameters to avoid area magnification errors caused by irregular boundaries. XPS peak fitting employed Shirley background subtraction and uniform peak width constraints, and surface F/Si atomic fractions were corrected using the same sensitivity factor.In contact angle measurements, if a single data point deviated by more than 5° from the rest of the data, it was deemed to indicate a local defect and was retested. The resulting surface energy, roughness, phase region size, cross-linking density, and surface element retention rate were not considered in isolation but collectively served as preliminary structural parameters for interpreting acid absorption behavior, electrochemical barrier performance, and corrosion failure pathways.

The test of acid absorption utilizes a protocol of weighing with timing. We take samples at 3, 6, 12, 24, 48, and 72 hours in the first soaking stage, then we carry out measurements at 5, 7, 10, 15, 20, and 30 d. Before every single weighing process, the surface of the free thin film was softly wiped by using lint-free paper under a fixed pressure for 5 seconds, in order to get rid of the effect brought by leftover liquid, after which the weighing work is done on an analytical balance. If the mass difference of the same sample in two continuous measurements was smaller than 0.2 mg, therefore it was regarded by us as having achieved a close-to-equilibrium adsorption state. The diffusion coefficient we fitted by only using the data segments that come from the initial period which satisfy the linear relationship, hence it ensures the comparability of transport parameters among different formulations.

## 2.3 Acid Corrosion Evaluation and Electrochemical Analysis

The evaluation of acid resistance consists of four parts: static immersion, interfacial adhesion retention, electrochemical impedance analysis, and corrosion morphology observation. A 5 wt% $H_2SO_4$solution was selected as the immersion medium, with the temperature controlled at 25 ± 1 °C and immersion times set at 1, 7, 15, and 30 d.This concentration was chosen to accelerate the differences among formulations in acid absorption, interfacial degradation, and under-film corrosion while ensuring a clear observation window for the coating structure. After immersion, the samples were rinsed with deionized water, surface droplets were removed with lint-free paper, and the samples were left at room temperature for 12 h before subsequent testing. Adhesion was tested using the peel test method, with no fewer than 3 parallel samples per group.To avoid any additional effects of residual acid on peel adhesion, all samples were

vacuum-dried at 40 °C for 2 h prior to testing. The adhesion retention rate is defined as shown in Equation (3).

$$R_A = \frac{A_t}{A_0} \times 100\% \tag{3}$$

where, $R_A$ is the adhesion retention rate after immersion for $t$ , and $A_0$ and $A_t$ are the peel strengths before and after immersion, respectively. Electrochemical testing was conducted using a classic three-electrode system in 0.1 mol·$L^{-1}$ $H_2SO_4$.The working electrode was a coated steel specimen with an exposed area of 1.0 $cm^2$; the reference electrode was a saturated calomel electrode; and the counter electrode was a platinum plate. Prior to testing, the samples were left to stand in the electrolyte for 30 min, and testing began once the open-circuit potential drift was less than 2 mV·$min^{-1}$. The EIS frequency range was$10^5$-$10^{-2}$Hz, with a perturbation amplitude of 10 mV. After 7 d of immersion and thereafter, when interfacial responses begin to appear in the low-frequency region, the analysis switches to a double-time-constant model fitting. To compare the decay rates of different formulations from the initial shielding phase to the long-term retention phase, this study characterizes the relative retention of the impedance modulus at 0.01 Hz, as shown in Equation (4).

$$\eta_Z = \frac{|Z|_{0.01\ \mathrm{Hz},t}}{|Z|_{0.01\ \mathrm{Hz},1d}} \times 100\% \tag{4}$$

where $\eta_Z$ is the low-frequency impedance retention rate after immersion for time $t$ , and $|Z|_{0.01\ \mathrm{Hz},1d}$ and $|Z|_{0.01\ \mathrm{Hz},t}$ are the impedance modulus values at 0.01 Hz after 1 day of immersion and immersion for time $t$ , respectively. This metric is used to describe the relative level of the film's ability to maintain its shielding capability in long-term acidic media, rather than substituting a high impedance value at a single point in time for an overall assessment of durability.

Electrochemical polarization was performed within a range of ± 250 mV around the open-circuit potential at a scan rate of 0.5 mV·$s^{-1}$.Test results are used to obtain corrosion current density and corrosion potential via Tafel extrapolation, which aids in comparing the degree of interfacial activation of different formulations in acidic media. Given that this study focuses on the barrier mechanism and interfacial stability of the coating, polarization parameters are considered only as part of the electrochemical evidence and are not used independently as criteria for acid resistance grading [21-24]. Correspondingly, the surface and cross-sectional morphologies after immersion were examined via SEM to identify failure features such as crack propagation, blister formation, and interfacial delamination; changes in surface elements were analyzed in conjunction with XPS results to determine whether the acid solution had penetrated the surface barrier and triggered interfacial reactions.

A staged model selection strategy was adopted for impedance spectroscopy fitting. If only a single broad peak appeared in the Bode phase diagram during the initial immersion stage, and the Nyquist plot exhibited a single compressed semicircle, the process was treated as film-dominated; when new characteristic peaks or additional arc segments appeared in the low-frequency region, the analysis switched to a dual-response model.All fittings are accepted if the criterion $\chi 2 < 10^{-3}$ is met, and the continuity and physical plausibility of parameter changes over time are verified [25]. Acid resistance is not determined based on a single impedance result but is comprehensively analyzed by combining low-frequency impedance retention, adhesion retention, and corrosion morphology.

The analysis of morphology after corrosion has been carried out in a quantitative way. The density of surface cracks is computed through the method of summing all crack lengths for each

unit area after image binarization; The blister's dimension is given by the equal diameter; and the width of delamination on cross-sections is gotten as the average value from five different positions. For each sample, we record at least three surface regions and three cross-section regions, with the goal to lower the deviation that the single observation field can bring. The correlation analysis that we conducted utilized surface F atom proportion, 30-day acid absorbing speed, cross-linking density, average phase area dimension, and surface free energy as input variant quantities. These have been matched with apparent diffusion coefficient, 30-day low-frequency impedance, and adhesion retention rate for the carrying out of analysis. We utilized the Pearson correlation coefficient for assessing the strength of trends, and we set the significance level to be 0.05.

All tests were conducted in a standardized sequence. For samples from the same batch, non-destructive tests such as contact angle, XPS, and EIS were performed first, followed by adhesion testing, cross-sectional brittle fracture analysis, and surface metallization observation. Independent samples were used for specimens collected at different stages to avoid additional stress introduced by soaking-drying cycles.All raw data were archived by sample number, batch number, and test date. Statistical results were reported as both mean and standard deviation. If a duplicate sample deviated from the group mean by more than two standard deviations in film thickness, initial adhesion, or open-circuit potential, the application and surface defect records were reviewed; upon confirmation of an anomaly, the sample was discarded and a replacement duplicate was prepared.

# 3 Results and Discussion

## 3.1 Nanostructure Evolution and Interfacial Physicochemical Regulation

To first address what structural changes occur when fluorosilicone components enter the epoxy network, this paper analyzes the system from three perspectives: chemical bond characteristics, nanophase distribution, and thermomechanical response, as shown in Figure 2.

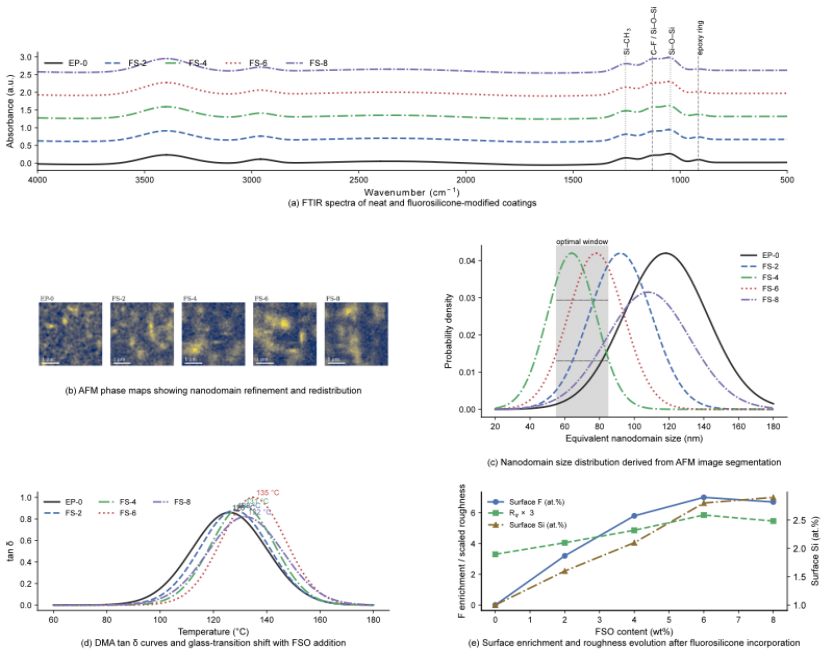


*Figure 2: FTIR spectra, AFM topography/phase maps, domain-size distributions, and DMA tan δ evolution of coatings with different fluorosilicone contents.*

In Figure 2, the characteristic Si-O-Si absorption in the FTIR spectra near 1100-1030 $cm^{-1}$gradually increases with rising FSO content, indicating that the siloxane backbone has incorporated into the cured film structure; correspondingly, the absorption associated with fluorinated segments is more pronounced in the modified samples, suggesting that low-surface-energy units were not completely masked during the curing process.Meanwhile, AFM phase maps and phase domain size distributions provide more direct structural evidence: compared to EP-0, the phase domains in FS-2 and FS-4 have become significantly finer, while the distribution peak in FS-6 has shifted further to the left and narrowed, indicating smaller and more concentrated nanoscale phase domains in this formulation;When the content increased to FS-8, the distribution curve shifted back toward larger sizes, suggesting that an excess of fluorosilicon components had begun to cause local phase aggregation. In other words, the effect of FSO is not linearly enhanced but forms a relatively stable nanoscale control window around the medium loading level.

This alteration is further got proof by the DMA curves. In Figure 2(d), the position of tanδ peak is gradually increased from about 126 °C for EP-0, it reaches around 135 °C at FS-6, and then it drops back to about 132 °C at FS-8. These findings show that a medium quantity of FSO cannot make the main network become weaker; instead, it raises the energy that is needed for segment movement by means of co-curing fixing and partial siloxane restriction. But, when the doping concentration keeps on rising, local phase separation and network non-uniformity start to offset this benefit. Figure 2(e) further shows that the degree of surface F and Si enrichment rises greatly as FSO content goes up, while roughness increases at the same time and becomes stable near 6 wt%. Through all-round analysis on Figures 2(a)-(e), we can know that FS-6 reaches a more balanced condition in three aspects of “surface enrichment-phase domain refinement-network constraint”, therefore it provides the structural precondition for the follow-up acid diffusion suppression and promoted electrochemistry retention ability. After we have confirmed that fluorosilicone components have entered the cured film and changed the nanoscale structure, therefore it is necessary to further judge whether this structural adjustment has truly become changes of surface wetting behavior and interfacial thermodynamic states, as what is shown in Figure 3.

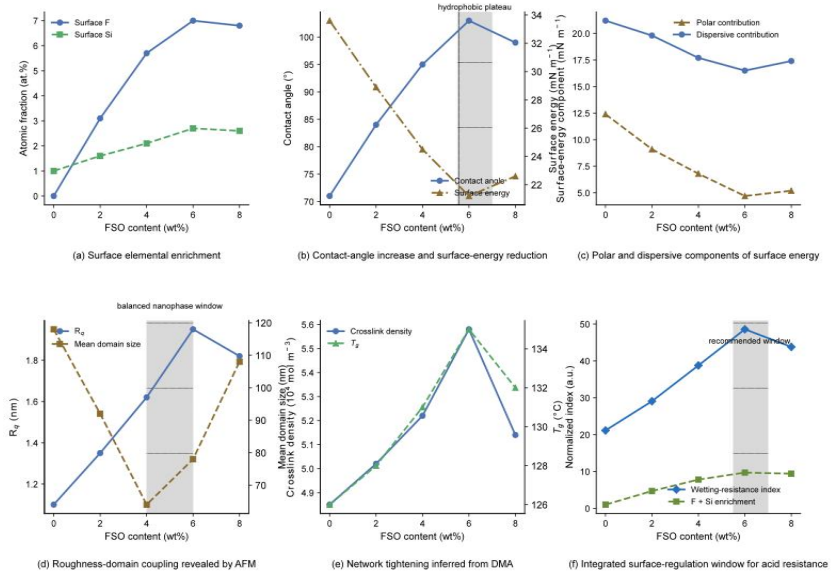


*Figure 3: Surface elemental enrichment, wetting behavior, surface-energy components, roughness/domain growth, and network-constraint metrics as a function of fluorosilicone content.*

Figure 3(a) shows that the surface F atom fraction increases continuously as the FSO content rises from 0 wt% to 6 wt%, reaching a maximum at FS-6, after which it essentially ceases to increase at FS-8; although the surface Si content also rises synchronously, the magnitude of change is smaller than that of F. This indicates that low-surface-energy segments exhibit a stronger tendency for surface migration, and that approximately 6 wt% is close to the enrichment limit.Consistent with this trend, Figure 3(b) shows that the contact angle increases continuously from approximately 72° for EP-0 to approximately 103° for FS-6, while the surface free energy decreases from approximately 34 $mN \cdot m^{-1}$to approximately 22 $mN \cdot m^{-1}$;when the formulation was further increased to FS-8, the contact angle dropped slightly, and the surface free energy ceased to decrease, indicating that the low-energy surface layer did not continue to improve after excessive incorporation.

Figure 3(c) further illustrates that the decrease in surface free energy primarily stems from the rapid weakening of the polar component, while changes in the dispersion component are relatively limited. This is particularly critical for acid resistance, as one of the prerequisites for acid penetration into the membrane is precisely the enhancement of surface wetting and polar interactions.Figures 3(d) and 3(e) link the surface state to the bulk structure: with the introduction of FSO, Rq increases from approximately 1.2 nm to around 1.9 nm, while the average phase domain size first decreases and then rebounds; the crosslinking density and glass transition temperature also reach high levels simultaneously in FS-6.In other words, FS-6 does not rely solely on stronger surface fluorination to reduce wetting, but rather achieves simultaneous optimization in three aspects: “weakened surface polarity, moderate phase domain size, and enhanced network constraints.”The comprehensive control window shown in Figure 3(f) illustrates this point: the 4-6 wt% range is the most suitable structural control zone, with 6 wt% corresponding to the optimal comprehensive acid resistance. Combined with the acid absorption and diffusion parameters in Table 2, it is evident that the nanostructure corresponding to 6 wt% FSO is most conducive to subsequent acid-resistant shielding, as shown in Table 2.

*Table 2: Physicochemical and thermomechanical parameters of the coatings*

| Sample | Surface F / at% | Domain size / nm | Water contact angle / ° | Surface free energy / $mN \cdot m^{-1}$ | Rq / nm | Tg / °C | Crosslink density / $10^3$ $mol \cdot m^{-3}$ | Acid uptake after 30 d / % | Diffusion coefficient / $10^{-10}$ $cm^2 \cdot s^{-1}$ |
|---|---|---|---|---|---|---|---|---|---|
| EP-0 | 0.0 | - | 78.4±1.3 | 34.8±0.7 | 12.6±1.1 | 129.1±0.8 | 4.82±0.09 | 5.84±0.18 | 28.3±1.4 |
| FS-2 | 6.1±0.4 | 24±6 | 91.7±1.5 | 28.9±0.6 | 18.5±1.4 | 131.4±0.9 | 5.06±0.11 | 4.72±0.16 | 21.9±1.2 |
| FS-4 | 9.8±0.5 | 43±9 | 103.6±1.2 | 23.7±0.5 | 26.9±1.7 | 134.8±0.7 | 5.35±0.10 | 3.96±0.14 | 15.8±0.8 |
| FS-6 | 12.7±0.6 | 61±12 | 112.8±1.0 | 19.6±0.4 | 34.2±2.1 | 138.6±0.6 | 5.79±0.12 | 2.87±0.10 | 7.6±0.5 |
| FS-8 | 13.1±0.7 | 118±25 | 108.9±1.4 | 21.1±0.5 | 49.7±2.8 | 132.7±0.8 | 5.11±0.13 | 4.11±0.15 | 16.2±0.9 |

## 3.2 Acid barrier performance and electrochemical response

After the structural and surface parameters had been confirmed, the next step was to judge whether these changes truly promoted the electrochemical shielding ability in an acid environment, just as it is displayed in Figure 4. This diagram displays the distinctions in protecting capability among different formulas under long-time soaking conditions from four angles: frequency-region resistance, phase reaction, Nyquist electric capacity curves, and low-frequency holding behavior.

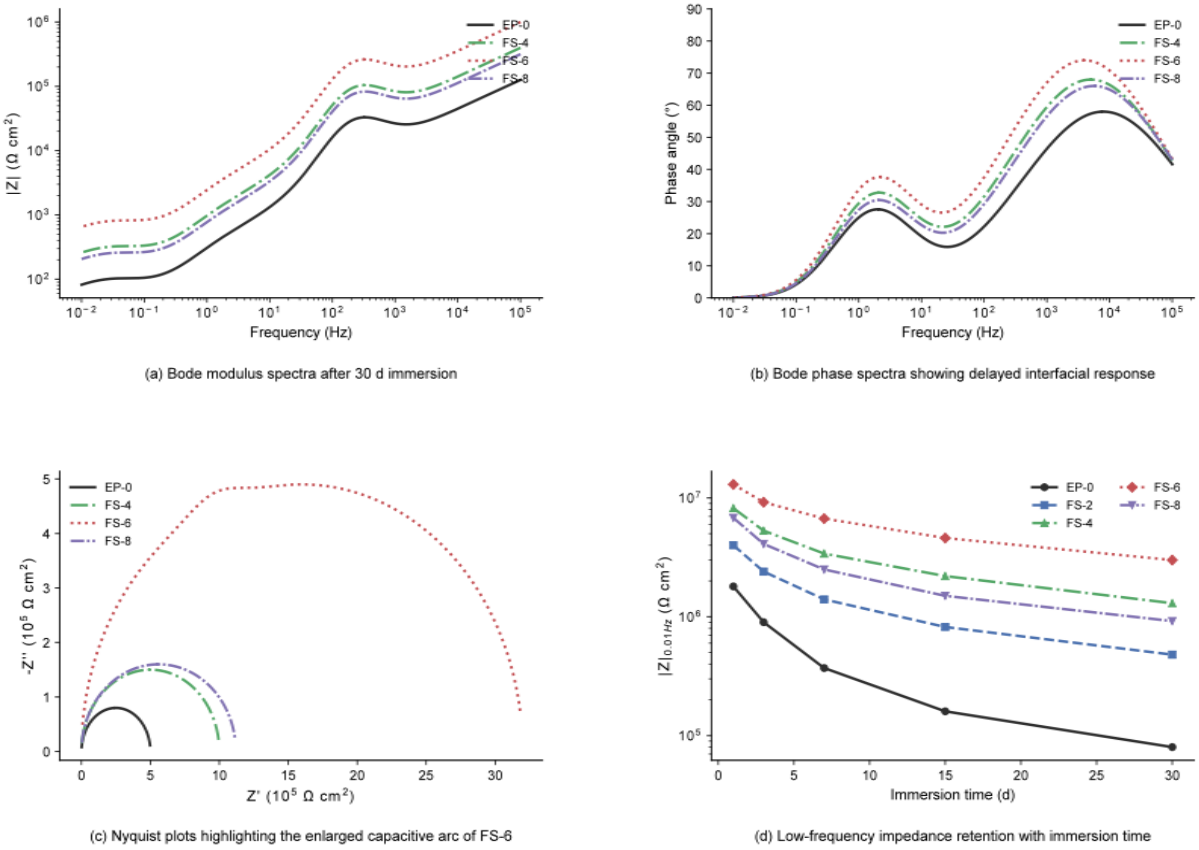


*Figure 4: Bode magnitude/phase plots, Nyquist plots, and time-dependent low-frequency impedance of coatings in an acidic medium.*

As shown in Figure 4(a), after 30 d of immersion, the $|Z|$ curves for each sample still exhibit clear stratification, with FS-6 maintaining the highest levels across the entire frequency range, followed by FS-4, then FS-8, while FS-2 and EP-0 are significantly lower.The difference in impedance magnitude in the low-frequency region is particularly striking, indicating that samples with moderate doping levels can maintain a more intact dielectric barrier pathway even after long-term immersion.In Figure 4(b), FS-6 exhibits a wider phase angle plateau and delayed low-frequency decay, indicating that the membrane-dominated response persists longer and the interfacial electrochemical process intervenes later; conversely, EP-0 shows a phase angle collapse at an earlier stage, suggesting that the acid solution has reached the metal interface more rapidly and triggered the corrosion process.

The Nyquist figure further makes stronger this conclusion. In the Figure 4(c), FS-6 displays the biggest radius of capacitive arc, and FS-4 also keeps a comparatively complete semicircle character, while EP-0 possesses the smallest arc section, therefore it indicates that its interfacial reaction resistance is obviously lower. In combination with Figure 4(d), we can discover that the low-frequency impedance of all samples continuously drops along with the immersion time, but the speeds of decline have obvious differences: EP-0 decreases quickly in the first 7 d and thereafter stays at a low level; FS-2 and FS-8, though they have improvement when compared with the unmodified sample, still display a continuous trend of going down; FS-4 and FS-6 display a clearly slower attenuation, with FS-6 keeping the highest low-frequency impedance degree even at 30 d. Nevertheless, the impedance results which we get alone are not enough to completely describe acid resistance; it is a necessary thing that we conduct analysis on interfacial polarization, acid absorption, and adhesion holding inside the identical frame, just like what is displayed in Figure 5.

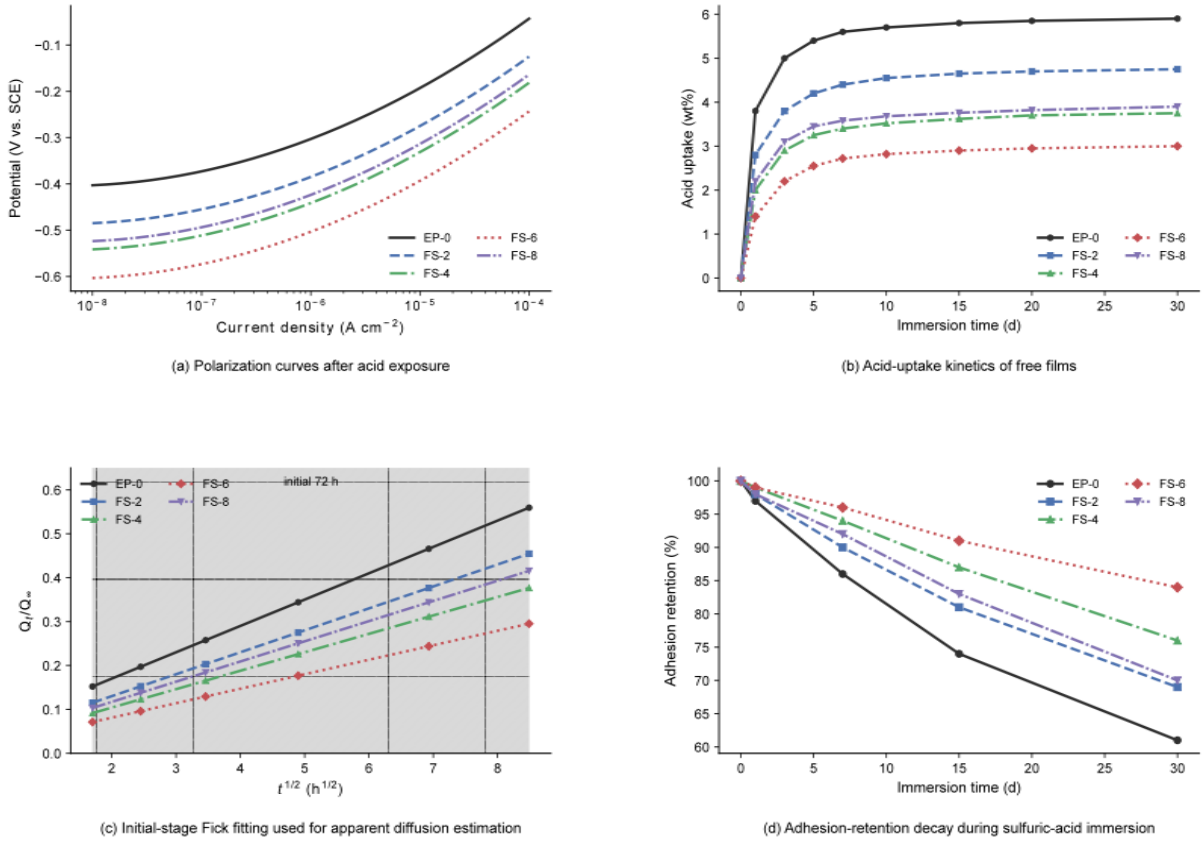


*Figure 5: Polarization curves, acid uptake kinetics, initial Fick fitting, and adhesion retention of coatings during acid immersion.*

In Figure 5(a), the polarization curves of the modified samples shift overall toward the region of lower current density, with FS-6 exhibiting the lowest current response, followed by FS-4, indicating weaker interfacial activation within the same potential range; the EP-0 curve is positioned farthest to the upper right, corresponding to a higher corrosion current density. This trend is consistent with the acid uptake behavior. Figure 5(b) shows that the acid absorption rate of EP-0 rises rapidly in the initial stage, approaching 5.8 wt% after 30 d;FS-6 exhibits the lowest absorption rate and final absorption amount, reaching only about 3.4 wt% at 30 d; FS-4 and FS-8 fall at an intermediate level, while the improvement in FS-2 remains limited. In other words, the introduction of fluorosilicon primarily alters the ease with which the acid solution penetrates the membrane layer, and this difference continues to be amplified during the middle and late stages of immersion.

The initial Fick fits shown in Figure 5(c) further illustrate this point. EP-0 exhibits the steepest slope, indicating the highest apparent diffusion coefficient; FS-6 has the flattest slope, suggesting the slowest early transport of the acid solution within the membrane layer. These results demonstrate that the combination of surface deactivation and regulation of the bulk nanophase region indeed jointly lengthens the transport path of the medium. Corresponding to the slowed transport, the rate of decline in adhesion retention over time, as shown in Figure 5(d), also differs significantly: EP-0 drops to approximately 60% after 30 d, FS-2 and FS-8 to approximately 68%-69%, FS-4 to approximately 76%, while FS-6 remains at approximately 82%.This implies that the advantage of FS-6 is not only reflected in the lower acid absorption of the membrane layer itself, but also in the significantly delayed decay of adhesion after the acid solution reaches the interface. A comprehensive analysis of Figures 5(a)-(d) reveals that an FSO content of approximately 6 wt% most effectively reduces the acid transport rate and

converts this initial advantage into a higher interfacial retention rate. To facilitate comparison of key corrosion resistance parameters for different formulations after long-term acid immersion, this paper summarizes low-frequency impedance, corrosion current density, apparent diffusion coefficient, 30-day acid absorption rate, and adhesion retention rate in Table 3.

*Table 3: Electrochemical fitting and corrosion parameters of coatings in acid medium*

| Sample | Ecorr / V | $i_{corr}$ / A·cm$^{-2}$ | Rpo / Ω·cm$^2$ | Rct / Ω·cm$^2$ | \|Z\|0.01Hz (1 d) / Ω·cm$^2$ | \|Z\|0.01Hz (30 d) / Ω·cm$^2$ | Adhesion retention after 30 d / % |
|---|---|---|---|---|---|---|---|
| EP-0 | -0.542 | $1.84\times10^{-6}$ | $1.25\times10^{4}$ | $2.97\times10^{4}$ | $3.20\times10^{6}$ | $1.70\times10^{5}$ | 61.2±2.3 |
| FS-2 | -0.476 | $6.73\times10^{-7}$ | $3.84\times10^{4}$ | $8.66\times10^{4}$ | $1.10\times10^{7}$ | $4.90\times10^{5}$ | 69.4±2.0 |
| FS-4 | -0.411 | $2.16\times10^{-7}$ | $1.25\times10^{5}$ | $3.12\times10^{5}$ | $3.70\times10^{7}$ | $1.80\times10^{6}$ | 77.8±1.8 |
| FS-6 | -0.301 | $3.92\times10^{-8}$ | $4.68\times10^{5}$ | $1.12\times10^{6}$ | $1.80\times10^{8}$ | $7.90\times10^{6}$ | 86.5±1.6 |
| FS-8 | -0.438 | $1.87\times10^{-7}$ | $9.73\times10^{4}$ | $2.68\times10^{5}$ | $6.40\times10^{7}$ | $8.60\times10^{5}$ | 71.3±2.1 |

In Table 3, FS-6 exhibits a superior combination of performance across several metrics-$|Z|_{0.01\ Hz}$, $i_{corr}$, $D$, acid absorption rate after 30 d, and adhesion retention rate-indicating that its moderate incorporation not only slows the rate of acid penetration into the membrane layer but also delays the onset of interfacial instability;Although FS-8 still outperforms the unmodified sample, its diffusion and retention indices have deteriorated, consistent with the earlier observation that excessive incorporation leads to coarsening of the phase structure.

## 3.3 Acid-induced degradation pathway and corrosion inhibition mechanism

To confirm the actual failure morphology corresponding to the electrochemical and acid absorption results, this study further compared the surface and interfacial evolution of different formulations after acid immersion, as shown in Figure 6.

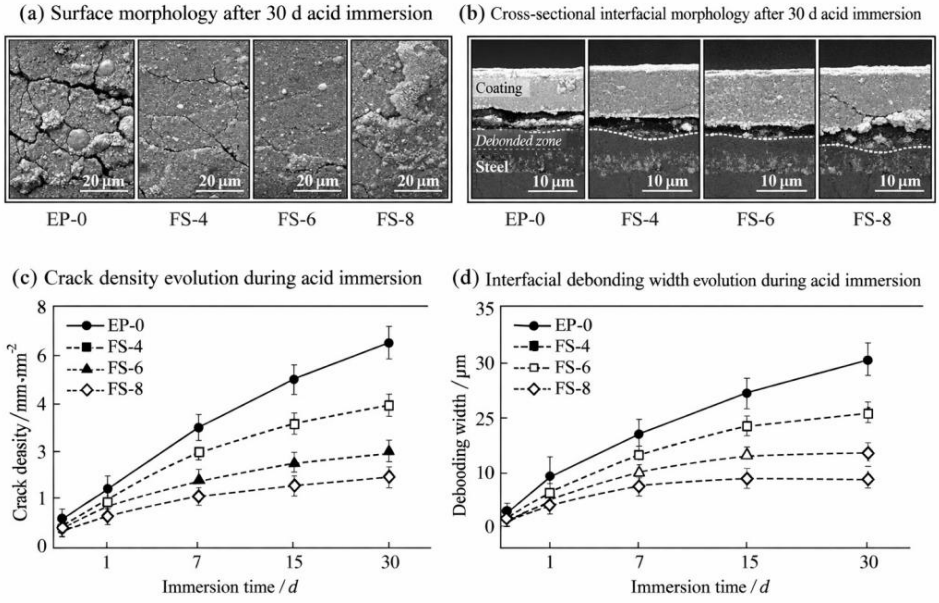


*Figure 6: Representative surface and cross-sectional morphologies and quantified crack/delamination evolution after acid immersion.*

In Figure 6(a), EP-0 exhibited more pronounced surface roughening, crack connectivity, and localized blistering after 30 d, indicating that acid penetration not only caused plasticization but also promoted the continuous expansion of surface defects;Surface damage in FS-4 has been significantly reduced; FS-6 maintains the most intact surface condition, with only a few scattered defects observed; although FS-8 performs better overall than EP-0, relatively coarse and heterogeneous regions are still visible locally, indicating that the coarsening of phase domains caused by excessive fluorosilicon components weakens the stability of the surface layer. The cross-sectional results are consistent with the surface observations.Figure 6(b) shows that EP-0 has the widest delamination zone at the interface, FS-6 the narrowest, and FS-4 and FS-8 fall within an intermediate range, indicating that the ability of the acid solution to propagate laterally along the interface is also regulated by the formulation.

This difference is even clearer in the quantitative results. In Figure 6(c), the crack density of EP-0 continues to rise with immersion time, reaching its peak at 30 d; FS-6 maintains the lowest growth rate throughout the entire process, followed by FS-4, while FS-8 exhibits a faster increase in the middle to late stages.Figure 6(d) shows that the order of increase in interfacial delamination width is generally consistent with that of crack density: EP-0 exceeded 30 μm at 30 d, FS-4 was approximately 13 μm, FS-8 was approximately 15 μm, while FS-6 remained controlled at approximately 5 μm.Building on the preceding results, it is necessary to consolidate surface enrichment, acid transport, network constraint, and long-term retention capacity into a single graph, as shown in Figure 7.

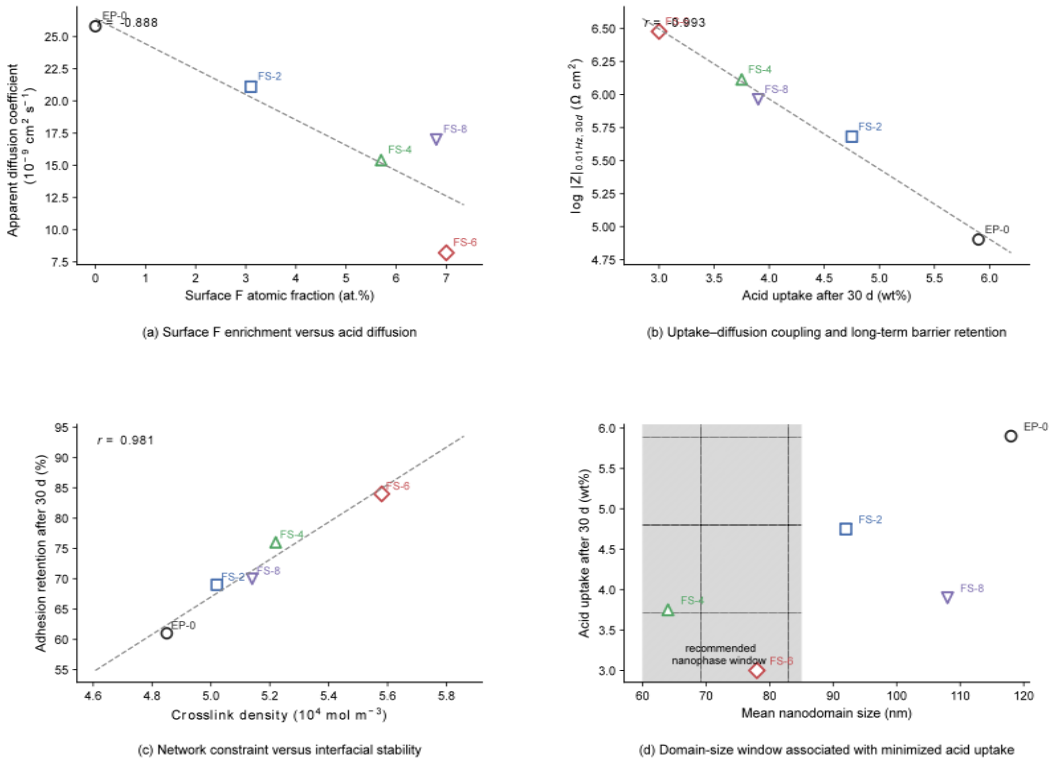


*Figure 7: Correlations among surface fluorine enrichment, acid transport, network constraint, and long-term barrier performance.*

Figure 7(a) makes clear that the surface fluorine atom proportion displays an obvious negative relation with the apparent diffusion coefficient, hence the correlation coefficient is $r = -0.888$. This illustrates that surface fluorine enrichment is not an independent ornamentation character, but rather directly corresponds to a reduction of the acid penetration speed. Figure

7(b) further gives evidence that a stronger negative correlativity exists between the acid absorption speed after 30 d and the low-frequency impedance. $r = -0.993$. Change another word to say, so long as the membrane layer keeps on absorbing acid, the long-term barrier property will quickly become bad, the two of them show an almost one-direction relation. On the opposite side, Figure 7(c) demonstrates a obvious positive connection between crosslinking density and the 30-day adhesion retention rate, $r = 0.981$, hence indicating that the strengthened bulk network limiting conditions therefore cause a simultaneous promotion for the stability of the interface inside an acidic medium.

Figure 7(d) shows us that there is an obvious size window belonging to the nanophase regions. When the average size of nanophase is too big, the rate of acid absorption at 30 d has a significant increase; when the dimension drops into the scope of about 75-85 nanometer, the acid absorption degree is the lowest, thus FS-6 is located exactly close to this interval. This result shows that acid resistance capability is not decided by only one high F content or only one high crosslinking density, but instead it depends on if “low-energy surface modification” and “moderate refinement of the bulk phase” are able to be reached at the same time. When the dimension of phase is excessively big, just like what is displayed for EP-0 and FS-8, local passages which enable medium to move are still comparatively easy to appear in the interior of the membrane; if enrichment and network restrictive conditions are optimized at the same time, acid diffusion, impedance retention, and interface adhesion can get synergistic improvement inside the same formulation. Therefore, 6 weight percent FSO is corresponding to an optimal structure and performance balance point, hence 4 weight percent lies inside a suboptimal range.

Based on the above-mentioned correlation results which have been gotten, this paper further combines the key failure stages in the acid corrosion process into one continuous mechanism, what is shown in Figure 8. Figure 8 is not simply a repetition of single test results, but it links the four stages-surface water wetting, diffusion inside the film, interface activation, and macro-scale damage-to give an explanation of why different formula systems show obviously different long-term acid resistance performance.

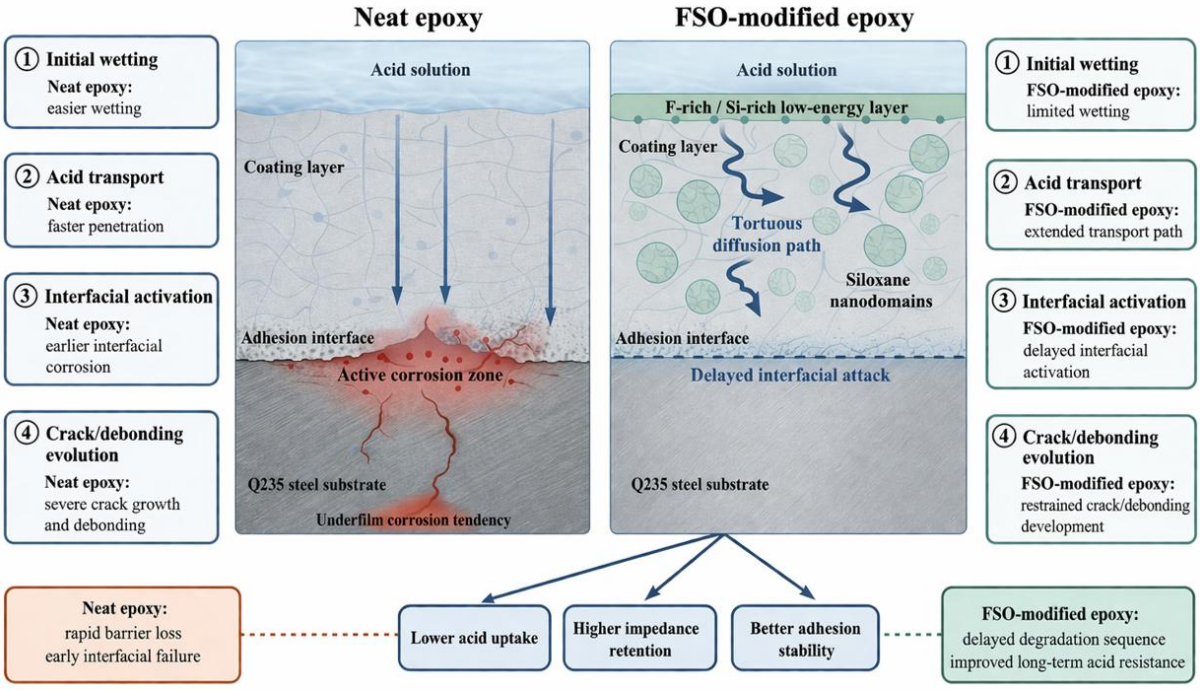


*Figure 8: Proposed degradation sequence and corrosion inhibition mechanism in an acidic medium.*

In Figure 8, the failure order of the unmodified epoxy paint can be concluded as below: the acid liquid first wets the surface comparatively simply and permeates into the coating layer, then spreads downward along a comparatively shorter moving path; after the medium arrives at the interface, the partial gathering of polar groups, the plasticization caused by acid, and the reactions on the interface gradually accumulate, hence finally displaying as crack extension, decreased adhesive force, and the starting of corrosion beneath the film. By comparison, the fluorosilicon-modified cover layer first forms a fluorine and silicon abundant low-energy stratum upon the surface, meanwhile it keeps a more fine-grained siloxane nanophase inside the bulk. These two compositions together lengthen the medium's transportation path, hence decreasing the effective diffusion speed of the acid liquid inside the thin film. The outcome is not the promotion of a single connection, but rather the synchronous postponement of the whole fault chain: surface moisture dipping becomes weaker, acid absorbing speeds get lower, and boundary layer activation is put off, hence finally holding down both crack density and delamination width.

# 4 Conclusion

This study focuses on the nanostructural regulation and acid corrosion resistance mechanisms of reactive fluorosilicon oligomer-modified epoxy coatings. Under a unified formulation, structural characterization, and acid medium evaluation protocol, a correlation was established between surface enrichment, bulk network, and interfacial failure, and the structural window corresponding to the optimal fluorosilicon content was identified. The main conclusions can be summarized as follows.

(1) Upon incorporation into the epoxy system, FSO forms a structural configuration during curing characterized by the coexistence of a surface layer enriched in fluorine and silicon and a continuous bulk cross-linked network. As the content increases from 0 to 6 wt%, the surface free energy continuously decreases, the nanophase region remains controllable, the cross-linking density and glass-transition temperature increase simultaneously, and the acid diffusion coefficient decreases significantly.

(2) A 6 wt% FSO content corresponds to the best acid resistance. After 30 d of acid immersion, this formulation still maintains a low-frequency impedance of $7.90\times10^{6}$ $\Omega\cdot cm^{2}$ and an adhesion retention rate of 86.5%, with the corrosion current density reduced to $3.92\times10^{-8}$ $A\cdot cm^{-2}$.The performance improvement stems from the synergistic effects of a stable low-energy surface layer, restricted diffusion pathways, and delayed interfacial reactions.

(3) An excess of fluorosilicon components leads to coarsening of the phase domain, enrichment of flexibility, and a decrease in structural continuity; acid resistance does not increase monotonically with the amount added. Future work is needed to further validate the long-term applicability of this structural window under more complex acid types, temperature fluctuations, and cyclic immersion conditions, combining in-situ impedance and nanomechanical characterization.

# About the Author

Fei Liu was born in Xiangfan, Hubei, PR China, in 1976. He received his bachelor's degree from Huazhong University of Science and Technology, PR China. He currently works at Shandong Nuclear Power Company. His main research area is thermal energy engineering in nuclear power plants.

Xin Wang was born in Tengzhou, Shandong, PRC, in 1985. He received his bachelor's

degree from Dalian University of Technology, PRC. He currently works in the Technical Support Department of Shandong Nuclear Power Company. His main research area is Materials Science and Anti-corrosion Engineering in Nuclear Power Plants.

# References

[1] Chruściel, J. J., & Leśniak, E. (2015). Modification of epoxy resins with functional silanes, polysiloxanes, silsesquioxanes, silica, and silicates. Progress in Polymer Science, 41, 67-121.

[2] Eduok, U., Faye, O., & Szpunar, J. (2017). Recent developments and applications of protective silicone coatings: A review of PDMS functional materials. Progress in Organic Coatings, 111, 124-163.

[3] Ge, Z. Y., Tao, Z. Q., Li, G., et al. (2011). Synthesis and properties of novel fluorinated epoxy resins. Journal of Applied Polymer Science, 120(1), 148-155.

[4] Yan, Z. L., Liu, W. Q., Wang, H. L., et al. (2014). Synthesis and characterization of a novel fluorinated siloxane star-like copolymer with a short perfluoroalkyl chain for the modification of epoxy resin. Journal of Fluorine Chemistry, 157, 63-72.

[5] Lim, J. S. K., Gan, C. L., & Hu, X. M. (2019). Unraveling the mechanistic origins of epoxy degradation in acids. ACS Omega, 4(6), 10799-10808.

[6] Yang, C., Wang, M., Yang, Z., et al. (2019). Investigation of the effects of acid, alkali, and salt solutions on fluorinated superhydrophobic surfaces. Langmuir, 35, 17027-17036.

[7] Zheng, X., Pang, A.-M., Wang, Y., et al. (2020). Fabrication of UV-curable fluorosilicone coatings with impressive hydrophobicity and solvent resistance. Progress in Organic Coatings, 142, 105633.

[8] Aparna, A., Sethulekshmi, A. S., Saritha, A., et al. (2022). Recent advances in superhydrophobic epoxy-based nanocomposite coatings and their applications. Progress in Organic Coatings, 166, 106819.

[9] Xu, L., Yang, X., Fu, X., et al. (2022). Fluorinated epoxy-based superhydrophobic coating with robust self-healing and anticorrosive properties. Progress in Organic Coatings, 171, 107045.

[10] Yang, Z., Bai, Y., Wei, B., et al. (2023). A facile preparation method of UV rapid curing fluorosilicone coatings with good hydrophobicity and excellent corrosion resistance based on thiol-ene click reaction. Progress in Organic Coatings, 174, 107248.

[11] Yang, B., Lu, P., An, Q., et al. (2023). Protective effect of silicone-modified epoxy resin coating on iron-based materials against sulfate-reducing bacteria-induced corrosion. Progress in Organic Coatings, 174, 107241.

[12] Zhang, J.-T., Hu, J.-M., Zhang, J.-Q., & Cao, C.-N. (2004). Studies of water transport behavior and impedance models of epoxy-coated metals in NaCl solution by EIS. Progress in Organic Coatings, 51(2), 145-151.

[13] Ji, W.-G., Hu, J.-M., Zhang, J.-Q., & Cao, C.-N. (2006). Reducing water absorption in epoxy coatings by incorporating silane monomers. Corrosion Science, 48(11), 3731-3739.

[14] Ji, W.-G., Hu, J.-M., Liang, L., et al. (2006). Water uptake of epoxy coatings modified with γ-APS silane monomer. Progress in Organic Coatings, 57(4), 439-443.

[15] Ji, W.-G., Hu, J.-M., Liang, L., et al. (2007). Improving the corrosion performance of epoxy coatings by chemical modification with silane monomers. Surface and Coatings Technology, 201(8), 4789-4795.

[16] Liu, X., Xu, X., Zhang, F., et al. (2022). A synergistic anti-corrosion system based on durable superhydrophobic F-$SiO_2$/epoxy coatings and self-powered cathodic protection. Journal of Materials Chemistry A, 10, 18616-18625.

[17] Doganci, M. D., & Sevinç, H. (2023). Investigation of superhydrophobic and anticorrosive epoxy coatings on different surfaces utilizing hydrophobized aluminum oxide nanoparticles. ACS Omega, 8(24), 21559-21570.

[18] Zhang, X.-F., Li, X.-D., Wang, N., et al. (2023). Robust superhydrophobic $SiO_2$/epoxy composite coating prepared by a one-step spraying method for corrosion protection of aluminum alloy: Experimental and theoretical studies. Materials & Design, 228, 111833.

[19] Bratasyuk, N. A., Latyshev, A. V., & Zuev, V. V. (2024). Water in epoxy coatings: Basic principles of interaction with polymer matrix and the influence on coating life cycle. Coatings, 14(1), 54.

[20] Zhu, J., Fan, H., & Wan, J. (2024). Solvent-free and UV-cured epoxy silicone coating with excellent wear resistance and antismudge properties. ACS Applied Materials & Interfaces, 16(27), 35494-35504.

[21] Pan, K., Yang, S., Tao, X., et al. (2024). Enhancing corrosion resistance and toughness of solvent-free epoxy coatings with low-viscosity fluorine-containing hyperbranched polyether. Progress in Organic Coatings, 187, 108149.

[22] Wang, K., Wang, C., Dong, Q., et al. (2024). Simultaneous enhancement of corrosion and abrasion resistance in epoxy resin coatings using novel hyperbranched amino-polysiloxanes. Progress in Organic Coatings, 196, 108680.

[23] Tao, Z. Q., Yang, S., Ge, Z. Y., et al. (2007). Synthesis and properties of novel fluorinated epoxy resins based on 1,1-bis(4-glycidylesterphenyl)-1-(3′-trifluoromethylphenyl)-2,2,2-trifluoroethane. European Polymer Journal, 43, 550-560.

[24] Liu, Z., Zhang, G., Liu, Z., et al. (2012). Synthesis and properties of an epoxy resin containing trifluoromethyl side chains and its cross-linking networks with different curing agents. Polymer Degradation and Stability, 97, 691-697.

[25] Sanchez-Amaya, J. M., Osuna, R. M., Bethencourt, M., et al. (2007). Monitoring the degradation of a high-solids epoxy coating by means of EIS and EN. Progress in Organic Coatings, 60, 248-254.